Received: 19 September 2022 | Revised: 12 December 2022 | Accepted: 9 January 2023

DOI: 10.1111/ffe.13949

SPECIAL ISSUE ARTICLE

FFEMS Fatigue & Fracture of Engineering Materials & Structures

WILEY

A higher order thermoelastic analysis of fatigue crack growth can assess crack tip shielding

Alonso Camacho-Reyes[1] | **Jose M. Vasco-Olmo**[1] | **M. Neil James**[2,3] | **Francisco A. Diaz**[1]

[1]Departamento de Ingeniería Mecánica y Minera, Universidad de Jaén, Jaén, Spain

[2]School of Engineering, Computing and Mathematics, University of Plymouth, Plymouth, UK

[3]Department of Mechanical Engineering, Nelson Mandela Metropolitan University, Port Elizabeth, South Africa

Correspondence
Alonso Camacho-Reyes, Departamento de Ingeniería Mecánica y Minera, Universidad de Jaén, Jaén, Spain.
Email: acreyes@ujaen.es

Funding information
Junta de Andalucía, Grant/Award Number: 1380786

Abstract

The present work uses a more accurate thermoelastic formulation than the classical equation, based on the inclusion of a higher order term, to analyze crack tip thermoelastic data. It is shown that this thermoelastic analysis (TSA) model can be fitted to the Christopher–James–Patterson crack tip field model and hence provides information on crack tip shielding. To validate the results of this analysis, stress intensity factors (SIFs) were compared with results obtained from digital image correlation (also fitted to the CJP model). A comparison was also made between these CJP-derived SIF values and those obtained using a purely elastic Irwin–Westergaard approach. A high level of agreement was observed between DIC and TSA results in assessing ΔK_{CJP} that is the net result of the driving and the shielding forces on the crack tip. The ability to assess shielding using TSA is a significant step forward in its potential use in a more accurate characterization of crack tip fields.

KEYWORDS

CJP model, crack tip fields, crack tip shielding, digital image correlation (DIC), thermoelastic stress analysis (TSA)

Highlights

1. A high-order thermoelastic formulation is used to evaluate the crack shielding phenomenon.
2. CJP model experimental implementation using crack tip thermoelastic data.
3. High level of agreement between TSA and DIC results in terms of ΔK_{CJP}.

1 | INTRODUCTION

Since the middle of the 20th century, linear elastic fracture mechanics (LEFM) has provided simple and useful mathematical tools for the analysis of fatigue cracks[1] and has led to the widespread use of the damage-tolerant approach to fatigue life prediction. In turn, this has provided improved mechanical component design as well as

statistically reliable fatigue lifing. However, the plastic zone induced by cracking mechanisms in ductile materials surrounds the crack and modifies the range of SIF used to characterize fatigue crack growth rate (FCGR) and, depending on the type of loading, for example, constant or variable amplitude loading—overload or underload—is a major contributor to underestimation or overestimation of fatigue life. This effect, originally called plasticity-induced closure[2,3] but more accurately described as plasticity-induced crack shielding[4] (because it may derive from influences other than simply crack face interaction), has been widely studied since it was reported and named by Elber in 1970.[2] More recent work, for example, by Pippan and Hohenwarter,[5] has considered issues such as the physical origin, the consequences for the experimental determination, and the prediction of the effective crack driving force for fatigue crack propagation.

Many other authors have examined the various problems and controversies surrounding fatigue crack closure (shielding), for example, Fleck and Smith,[6] James and Knott,[7] James,[8] Allison et al.,[9] Jones et al.[10] In terms of more completely identifying potential mechanistic and mechanical contributions to plasticity-induced shielding, full-field optical experimental techniques have been demonstrated to be very efficient in quantifying the effective driving force for crack growth and in underpinning the development of more advanced models to describe the crack tip field and crack-shielding effect. Thus, the fatigue and fracture literature contains an extensive body of work that has used photoelasticity,[11,12] digital image correlation (DIC),[13–15] Moiré interferometry,[16] or thermoelastic stress analysis (TSA)[17,18] to analyze these phenomena.[19,20] Thermoelastic stress analysis (TSA)[17] has also been shown to be a linear elastic technique that can measure the effective fatigue crack driving force, for example, Diaz et al.[20]

The development of full-field experimental techniques capable of measuring crack tip fields has also made it possible to propose advanced models for these fields that more completely identify and incorporate the various effects that cause plasticity-induced shielding. Hence, the novel mathematical crack tip model developed by Christopher, James, and Patterson (known as the CJP model)[21–23] describes the crack tip singularity in terms of three stress intensity factors, one of them representing the sum of the driving forces for crack growth (K_F) that acts perpendicular to the crack plane and is assessed at the crack tip, while other two SIFs incorporate effects related to the plastic enclave that encloses the crack and that leads to the plasticity-induced shielding. This model was originally developed for stress fields and validated against photoelastic data[21,22] but was subsequently extended to DIC and displacement fields allowing its extension to metallic alloys.[23] It has been shown that the CJP model characterizes the effective fatigue crack driving force over a wider range of SIF that the standard Paris parameter ΔK, through the parameter ΔK_{CJP} that is defined in the paper by Vasco-Olmo et al.[24] as

$$\Delta K_{CJP} = (K_{F,max} \pm K_{R,max}) - (K_{F.min} \pm K_{R,min}). \quad (1)$$

It is important to note that negative signs for K_R in the CJP model have a real meaning as, from the definition of this parameter,[24] it can either assist or retard fatigue crack growth. The effective SIF range given by Equation (1) rationalizes fatigue crack growth rates across a range of stress ratios and specimen types.[25] This improved characterization of crack growth rate using elastic stress intensity factors is believed to reflect the way that the stress intensity parameters are defined at the crack tip (geometry independence) and the more accurate incorporation of plasticity effects that lead to shielding (plastic constraint effects at the elastic–plastic boundary and shear-induced transport of material from the crack wake to the crack tip[26]).

Thus, the CJP model also demonstrates an improved ability to characterize the plastic zone contour compared with other linear elastic models.[27] Further support for the validity of the model has come from work done by Nowell and Nowell[28] which used DIC to measure near-tip displacements, from which key parameters governing crack growth were extracted and used to validate the Pommier and Hammam[29] and CJP[23] models of fatigue crack deformation. Their conclusion was that both models represented similar approaches to capturing the effects of plasticity. It should be noted, however, that the formulation of the two models and their approach to the influences of plasticity are rather different. As noted in the conclusions of Nowell et al.'s work,[28] these two models demonstrate a capability of full-field techniques in combination with elastic–plastic modelling, captured in a two-term expression for near-tip deformation and stress, that may offer a promising approach for characterizing fatigue crack growth under more complex loading histories.

In the present work, the CJP model is applied to the analysis of TSA data via a second-order thermoelastic equation that includes shielding effects arising from the plastic enclave. This second-order thermoelastic formulation allows the temperature variation during loading to be correlated with the five CJP model coefficients that characterize the crack tip singularity. Experimental TSA data have also been used to compare values of the CJP model stress intensity K_F with the standard Irwin–Westergaard value of K_I at different crack lengths. DIC data were further used in combination with the CJP model to validate and compare the CJP crack tip

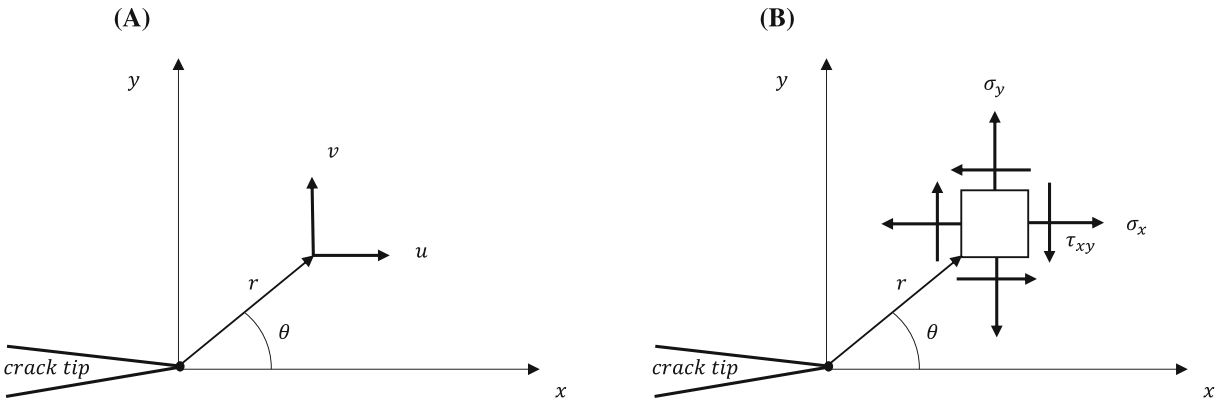

FIGURE 1 (A) Displacement field components and (B) stress tensor components in a point surrounding the crack tip in terms of the polar coordinates

parameters obtained with TSA since as previously reported, DIC is a well-stablished technique to assess crack shielding effects through the CJP model. Although finite element analysis is extremely useful and can provide stress values and subsequently determine the temperature range, a comprehensive numerical model would pose difficulties in reproducing nonlinear effects that arise from the inclusion of a plastic enclave in the elastic stress field, while experimental data are more definitive.

2 | THEORETICAL BACKGROUND

2.1 | Irwin–Westergaard crack tip field model

The Irwin–Westergaard model[30,31] is a linear elastic model that describes the crack tip singularity field using the stress tensor components given by Equations (2)–(4), where K_I is the opening mode stress intensity factor, K_{II} is the in-plane shear mode stress intensity factor, T_x is the nonsingular stress along the crack growth direction (x), and r and θ are a set of polar coordinates in the crack plane (see Figure 1).

$$\sigma_x = \frac{K_I}{\sqrt{2\pi r}}\cos\frac{\theta}{2}\left(1-\sin\frac{\theta}{2}\sin\frac{3\theta}{2}\right) - \frac{K_{II}}{\sqrt{2\pi r}}\sin\frac{\theta}{2}\left(2+\cos\frac{\theta}{2}\cos\frac{3\theta}{2}\right)+T_x, \tag{2}$$

$$\sigma_y = \frac{K_I}{\sqrt{2\pi r}}\cos\frac{\theta}{2}\left(1+\sin\frac{\theta}{2}\sin\frac{3\theta}{2}\right) + \frac{K_{II}}{\sqrt{2\pi r}}\sin\frac{\theta}{2}\cos\frac{\theta}{2}\sin\frac{3\theta}{2}, \tag{3}$$

$$\tau_{xy} = \frac{K_I}{\sqrt{2\pi r}}\sin\frac{\theta}{2}\cos\frac{3\theta}{2}+\frac{K_{II}}{\sqrt{2\pi r}}\cos\frac{\theta}{2}\left(1-\sin\frac{\theta}{2}\sin\frac{3\theta}{2}\right). \tag{4}$$

2.2 | CJP crack tip field model

The CJP model[21–23] is a mathematical model that describes the crack tip singularity field based on Muskhelishvili complex potentials theory.[32] This linear-elastic model considers the effect of the plastic enclave on the global elastic field by taking into account any crack face contact forces as well compatibility-induced forces along the elastic–plastic boundary that arise from the Poisson's ratio differences in the elastic and plastic regions. James et al.[23] describe these forces and their origin in some detail and provide a schematic force diagram to illustrate their action on the elastic and plastic regions. The stress components surrounding the crack tip are described through five coefficients as a function of a set of polar coordinates, with the coordinate origin located at the crack tip. The components of the plane stress tensor are given by Equations (5)–(7).

$$\sigma_x = \frac{1}{\sqrt{r}}\left\{-\frac{1}{2}(A+4B+8E)\cos\frac{\theta}{2}-\frac{1}{2}B\cos\frac{5\theta}{2} - \frac{1}{2}E\left[\ln(r)\left(\cos\frac{5\theta}{2}+3\cos\frac{\theta}{2}\right) + \theta\left(\sin\frac{5\theta}{2}+3\sin\frac{\theta}{2}\right)\right]\right\}+C, \tag{5}$$

$$\sigma_y = \frac{1}{\sqrt{r}}\left\{\frac{1}{2}(A-4B-8E)\cos\frac{\theta}{2}+\frac{1}{2}B\cos\frac{5\theta}{2} + \frac{1}{2}E\left[\ln(r)\left(\cos\frac{5\theta}{2}-5\cos\frac{\theta}{2}\right) + \theta\left(\sin\frac{5\theta}{2}-5\sin\frac{\theta}{2}\right)\right]\right\}-F, \tag{6}$$

$$\tau_{xy} = \frac{1}{\sqrt{r}}\left[\frac{1}{2}\left(A\sin\frac{\theta}{2} + B\sin\frac{5\theta}{2}\right) - E\sin\theta\left(\ln(r)\cos\frac{3\theta}{2} + \theta\sin\frac{3\theta}{2}\right)\right]. \quad (7)$$

In these equations, A, B, C, E, and F are the coefficients that describe the stress field and r and θ the polar coordinates. These coefficients are related with the crack tip parameters (stress intensity factors and nonsingular stresses) as shown in Expressions (8)–(12).

$$K_F = \sqrt{\frac{\pi}{2}}(A - 3B - 8E), \quad (8)$$

$$K_S = \sqrt{\frac{\pi}{2}}(A + B), \quad (9)$$

$$K_R = -(2\pi)^{3/2}E, \quad (10)$$

$$T_x = -C, \quad (11)$$

$$T_y = -F. \quad (12)$$

K_F is the opening mode stress intensity factor that sums the driving forces for crack growth, K_S is the stress intensity factor characterizing the interfacial shear stress, and K_R is a stress intensity factor that characterizes the direct stress opposing or retarding crack growth parallel with the crack growth direction. It can be either negative or positive in value and hence may act to either retard or accelerate crack growth as observed in the definition of ΔK_{CJP} (Equation 1). T_x and T_y are the nonsingular stresses in the crack growth (x) and crack opening (y) directions, respectively. The original model formulation considered six coefficients to describe the crack tip singularity field but assumed that $D = -E$ in order to model the asymptotic behavior of the stress along the crack flanks.[23] The CJP model gives the displacement field surrounding the crack tip through Equation (13):

$$2G(u + vj) = \kappa\left[-2(B + 2E)z^{\frac{1}{2}} + 4Ez^{\frac{1}{2}} - 2Ez^{\frac{1}{2}}\ln(z) - \frac{C - F}{4}z\right] - z\left[-(B + 2E)\bar{z}^{\frac{-1}{2}} - E\bar{z}^{\frac{-1}{2}}\overline{\ln(z)} - \frac{C - F}{4}\right] - \left[A\bar{z}^{\frac{1}{2}} - E\bar{z}^{\frac{1}{2}}\overline{\ln(z)} + 2E\bar{z}^{\frac{1}{2}} + \frac{C + F}{2}\bar{z}\right], \quad (13)$$

where u and v are the displacement field components, $j = \sqrt{-1}$, κ is a function of Poisson's coefficient, z is a complex variable ($r(\cos\theta + j\sin\theta)$), and the overbar denotes the complex conjugate.

2.3 | Thermoelastic stress analysis

Thermoelastic stress analysis (TSA) is based on the thermoelastic effect first reported by Kelvin.[17] When a solid is cyclically loaded under adiabatic and reversible conditions, a temperature change occurs in the solid that is related to the cyclic range of the first stress invariant. Considering a plane stress state, the classical TSA equation is given by Equation (14).

$$\frac{\Delta T}{T_0} = \gamma(\Delta\sigma_I + \Delta\sigma_{II}). \quad (14)$$

In this equation, ΔT is the peak-to-peak value of the temperature signal, T_0 is a reference temperature corresponding with the reference state of the solid, which, in this paper, is taken as the mean temperature on the solid surface, the Δ symbol indicates the range during a loading cycle, σ_I and σ_{II} are the principal stresses, and γ is a constant that depends on the specific heat, the thermal expansion coefficient, and the density. This equation describes the temperature range from only one term that is related to the first stress invariant range. However, this simplified equation is insufficiently accurate when there is a mean stress effect and, hence, high-order terms effect is not negligible.[33] Therefore, for a better modelling of the thermoelastic effect, a higher order term should be added to Equation (14). The inclusion of this term, governed by the second-order stresses, implies adding an additional constant b.[33–35] According to the formulation of Di Carolo et al.,[36] the normalized temperature range during a loading cycle considering two terms is given by Equation (15).

$$\frac{\Delta T}{T_0} = \gamma(\Delta\sigma_I + \Delta\sigma_{II}) + bR_f\left(-2\nu\Delta\sigma_I\Delta\sigma_{II} + \Delta{\sigma_I}^2 + \Delta{\sigma_{II}}^2\right), \quad (15)$$

where R_f is a function of the R ratio ($(1-R)/(1+R)$) and ν is Poisson's coefficient. From the relationships between the principal and Cartesian stress components derived from the stress invariants, Equation (15) can be expressed in terms of the components of a generic Cartesian stress tensor as shown in Equation (16).

$$\frac{\Delta T}{T_0} = \gamma\left(\Delta\sigma_x + \Delta\sigma_y\right) + bR_f\left(-2\nu\left(\Delta\sigma_x\Delta\sigma_y - \Delta\tau_{xy}^2\right) + \Delta\sigma_x^2 + \Delta\sigma_y^2 + 2\Delta\tau_{xy}^2\right). \quad (16)$$

3 | EXPERIMENTAL DETAILS

The experimental verification of the concept used a pure grade 2 titanium compact-tension specimen tested under

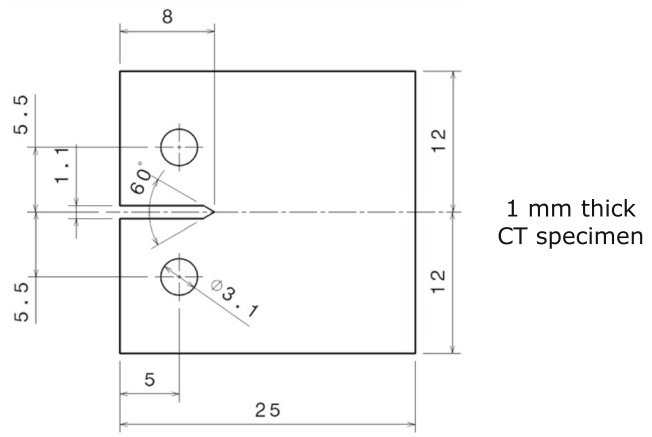

FIGURE 2 Dimensions of CT-specimen

TABLE 1 Mechanical properties for pure grade 2 titanium[25]

Mechanical property	Units	Value
Young modulus	GPa	105
Yield stress (0.2%)	MPa	390
Ultimate tensile stress	MPa	448
Elongation at failure	%	20
Poisson's coefficient	Dimensionless	0.34

constant amplitude cyclic loading at 11 Hz with stress ratios of either 0.1 or 0.6. In both cases, the maximum load was 750 N. Specimen dimensions are shown in Figure 2, while material properties and chemical composition are given in Tables 1 and 2, respectively. Thermal properties are displayed in Table 3. As shown in Table 3, the material thermal diffusivity, which is an indicator of the internal material adiabaticity, is 6.95 mm^2/s. In addition, the cyclic frequency used helps to avoid any risk of heat dissipation, thus ensuring adiabatic conditions under linear elastic conditions. An MTS Landmark 370.02 servohydraulic testing machine was used in the work. For DIC image acquisition, a CCD Marlin 2MPix camera was used fitted with a macro-zoom lens (MLH-10X EO) to increase resolution. The experimental setup is shown in Figure 3. One side of the specimen was painted with matt black paint to increase the surface emissivity for TSA, and the other side was painted with a stochastic speckle pattern of black on white. Temperature data were recorded over intervals of 22 loading cycles (2 s) at the maximum frame rate (300 Hz). Thus, 27 points were acquired per cycle. For data acquisition, a 2-ms integration time was selected, and DIC images were recorded at the end of each thermal data acquisition interval by applying a cyclic load and capturing 20 images per cycle. This process was repeated at intervals during the test, and data were recorded at a variety of different crack lengths in the interval from 5 to 10 mm.

To obtain the thermal calibration constants, an initial test was performed. In this case, a flat plate was tested under several stress conditions for different ratios between alternating and mean stress components. Data acquisition parameters were the same as those used in the fatigue test. The calibration loading conditions and calibration process are described in detail in the following section.

4 | EXPERIMENTAL DATA PROCESSING AND CRACK TIP PARAMETER DETERMINATION

4.1 | Determination of crack tip thermoelastic data and singularity parameters

Figure 4 illustrates the concept of acquiring a sequence of temperature map data during the measurement interval of 2 s over a complete load cycle. The basic concept is that an initial map is acquired at time $t = t^1$ and subsequent maps are acquired at specific intervals until time $t = t^k$. Figure 5 presents experimental data for the temperature variation measured through the loading cycle interval of 2 s and the result of fitting these data to a Fourier series (Equation 17).

$$T(t) = T_0 + M_r t + \sum_{i=1}^{\infty} M_i \sin(i\omega t + \phi_i). \quad (17)$$

Here, $T(t)$ is the temperature signal, T_0 is the reference temperature, M_r is temperature rate, M_i is the temperature amplitude of the i^{th} harmonic, ω is the circular frequency, and ϕ_i is the phase of the i_{th} harmonic. The coefficient M_r can be also included in the model fitting of mean temperature variations during the acquisition process.[36] However, provided that the acquisition time is around 2 s and the laboratory temperature is constant, this term can be neglected without affecting the results.

Fitting the experimental data to Equation (17) leads to solving a nonlinear problem, and the use of numerical methods requires an initial solution. To avoid this problem, it is convenient to rewrite the Fourier series in its trigonometric form (Equation 18) instead of the compact form (Equation 17).

$$T(t) = T_0 + M_r t + \sum_{i=1}^{\infty} (m_i \sin(i\omega t) + n_i \cos(i\omega t)). \quad (18)$$

Thus, the amplitude and the phase of each harmonic are then defined through the coefficients m_i and n_i as shown in Equations (19) and (20):

TABLE 2 Chemical composition for pure grade 2 titanium[25]

Element (wt %)	Fe	C	N	O	H	Ti
Standard	<0.20	≤0.08	≤0.05	≤0.20	≤0.015	Balance
Specimen	0.10	0.01	<0.01	0.12	0.002	Balance

TABLE 3 Thermal properties and density for pure grade 2 titanium[37]

Specific heat	Thermal conductivity	Density[a]	Thermal diffusivity
523 J/kg K	16.4 W/m K	4.51 g/cm^3	6.95 mm^2/s

[a]Density is included here due to its influence on thermal diffusivity.

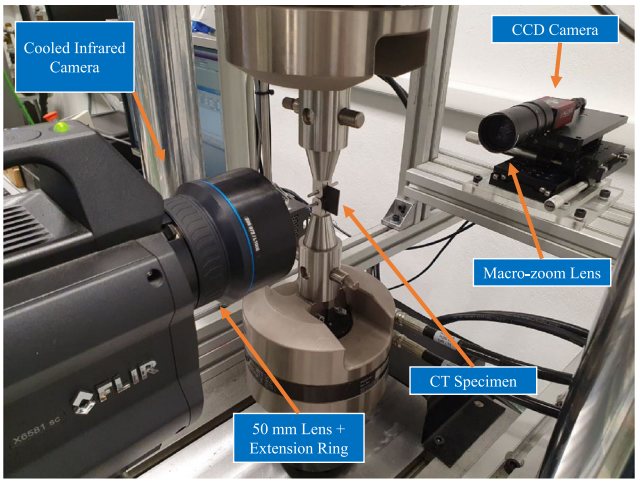

FIGURE 3 Experimental setup for DIC and TSA measurements [Colour figure can be viewed at wileyonlinelibrary.com]

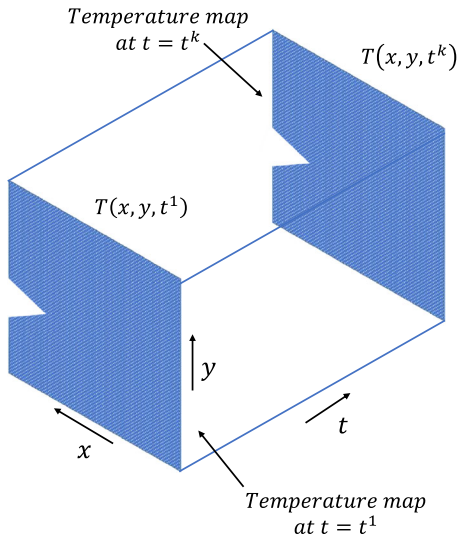

FIGURE 4 Illustration of the acquisition of temperature data during an interval of time [Colour figure can be viewed at wileyonlinelibrary.com]

$$M_i = \sqrt{m_i^2 + n_i^2}, \tag{19}$$

$$\phi_i = \arctan\left(\frac{m_i}{n_i}\right). \tag{20}$$

The trigonometric form of the Fourier series allows determination of the amplitude as well as the phase of each harmonic through solving a system of equations as shown in Equation (21):

$$\begin{bmatrix} 1 & t^1 & \sin(\omega t^1) & \dots & \sin(i\omega t^1) & \cos(\omega t^1) & \dots & \cos(i\omega t^1) \\ 1 & t^2 & \sin(\omega t^2) & \dots & \sin(i\omega t^2) & \cos(\omega t^2) & \dots & \cos(i\omega t^2) \\ 1 & t^3 & \sin(\omega t^3) & \dots & \sin(i\omega t^3) & \cos(\omega t^3) & \dots & \cos(i\omega t^3) \\ \vdots & \vdots & \vdots & \vdots & \vdots & \vdots & \vdots & \vdots \\ \vdots & \vdots & \vdots & \vdots & \vdots & \vdots & \vdots & \vdots \\ \vdots & \vdots & \vdots & \vdots & \vdots & \vdots & \vdots & \vdots \\ \vdots & \vdots & \vdots & \vdots & \vdots & \vdots & \vdots & \vdots \\ 1 & t^k & \sin(\omega t^k) & \dots & \sin(i\omega t^k) & \cos(\omega t^k) & \dots & \cos(i\omega t^k) \end{bmatrix}$$

$$\begin{bmatrix} T_0 \\ M_r \\ m_1 \\ \vdots \\ m_i \\ n_1 \\ \vdots \\ n_i \end{bmatrix} = \begin{bmatrix} T^1 \\ T^2 \\ \vdots \\ \vdots \\ \vdots \\ \vdots \\ \vdots \\ T^k \end{bmatrix}, \tag{21}$$

where superscripts 1 to k indicate time while subscripts 1 to i indicate the term number. Employing a suitable matrix factorization, the Fourier series coefficients can then be calculated. The fit quality was assessed via the Pearson correlation coefficient (the ratio of the covariance and the product of the standard deviations) between

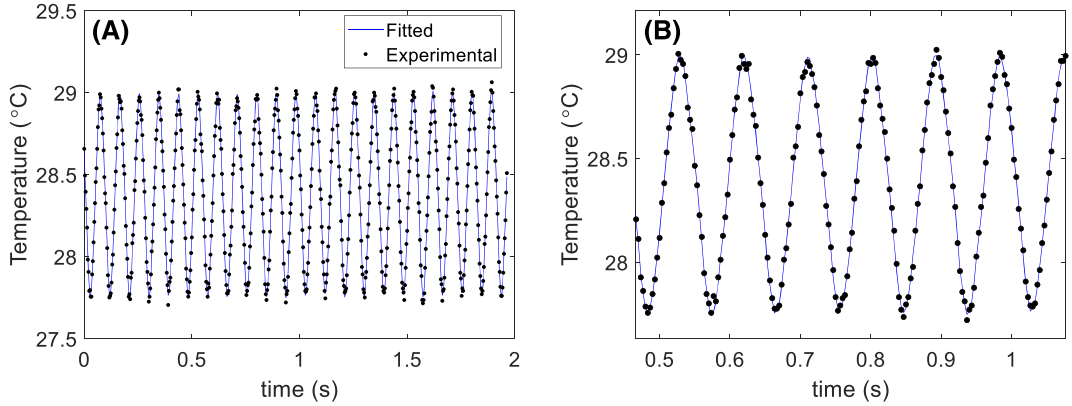

FIGURE 5 Measured temperature data at a point near the crack tip and the cyclic variation obtained through fitting it to a Fourier transform. (A) Temperature data for all cycles recorded over the 2-s measuring interval and (B) an expanded part of the data to demonstrate the quality of fit [Colour figure can be viewed at wileyonlinelibrary.com]

the measured and fitted data. Initially, 10 terms were employed to model the temperature signal. However, only the first harmonic amplitude is significant since the other harmonic amplitudes are considerably small and thus negligible. As illustrated in Figure 5, the temperature data in the elastic region during the cyclic loading show an almost perfect sinusoidal form, which explains why higher order harmonics are very close to zero in the bulk of the specimen far from the high-strain zone where linear elastic conditions exist. In fact, as reported by Pitarresi and Cappello,[38] the temperature second harmonic is clearly visible near the crack tip and along the crack flanks immediately behind the crack tip but is not significant beyond these zones. Figure 6 shows the calculated first harmonic temperature amplitude maps and Pearson correlation coefficient maps for the two stress ratios of 0.1 and 0.6.

Figure 6 shows that the temperature change is lower for $R = 0.6$ than at $R = 0.1$. As the maximum value of cyclic load was constant for both stress ratios, this correlates with the decrease in stress intensity change at $R = 0.6$ compared with $R = 0.1$ due to the higher minimum load at $R = 0.6$. This can be observed in both the temperature amplitude (first harmonic) data and in the maps of the Pearson correlation coefficient. Both types of data also contain information on the different crack tip stress zones, particularly the correlation coefficient maps. The crack tip singularity zone is identified with a correlation coefficient >70%, since smaller values imply that temperature values do not present a sinusoidal form when plotted against time. This value of 70% is derived from Figure 6C,D. As shown in these figures, there is a rapid decrease in Pearson's coefficient in the region from 70% to 35%. Moreover, if both fitted and experimental temperature signals are plotted, the agreement between them is very good in this region. Then, it starts to decrease when the singularity no longer affects the field since, although the rest of the specimen is experienced a stress cycle, these do not contribute to the temperature amplitude. Moreover, the specimen edge-affected zone is also recognized since in that zone, the temperature amplitude increases again. This can be observed in Figure 7 which plots a temperature amplitude profile (peak-mean signal value) for $\theta = 0$ (temperature profile ahead of the crack tip and along the crack growth or horizontal direction).

The data in Figure 7 also provide information about the different zones surrounding the crack tip. The maximum temperature amplitude can be considered as corresponding with the crack tip. The next zone corresponds to a high-strain plastic zone where nonlinear effects govern the stress field and the temperature decreases. Then, a trend change is observed where LEFM parameters govern the stress intensity ($\Delta T \propto r^{-1/2}$) until the temperature amplitude increases again due to specimen edge effects (that last zone in Figure 7 corresponds to the zone immediately near to specimen edge). The initial region in the left part of Figure 7, where an initial temperature increase is followed by a decrease, reflects heat dissipation arising from high-stress gradients near the crack tip and crack edge effects. Figure 7B shows a temperature profile along the crack growth direction for a stress ratio of 0.6. Figure 7A shows that the same zones also occur at the lower stress ratio of 0.1. However, the temperature profile for the high-stress ratio is noisier than for the low-stress ratio. This would be expected because smaller temperature changes (smaller loading amplitudes) imply noisy measurements.

To calculate the crack tip singularity parameters from the temperature amplitude maps, the Multi-point Over-Deterministic Method (MPODM) developed by Sanford and Dally[39] was employed. However, to remove the effect

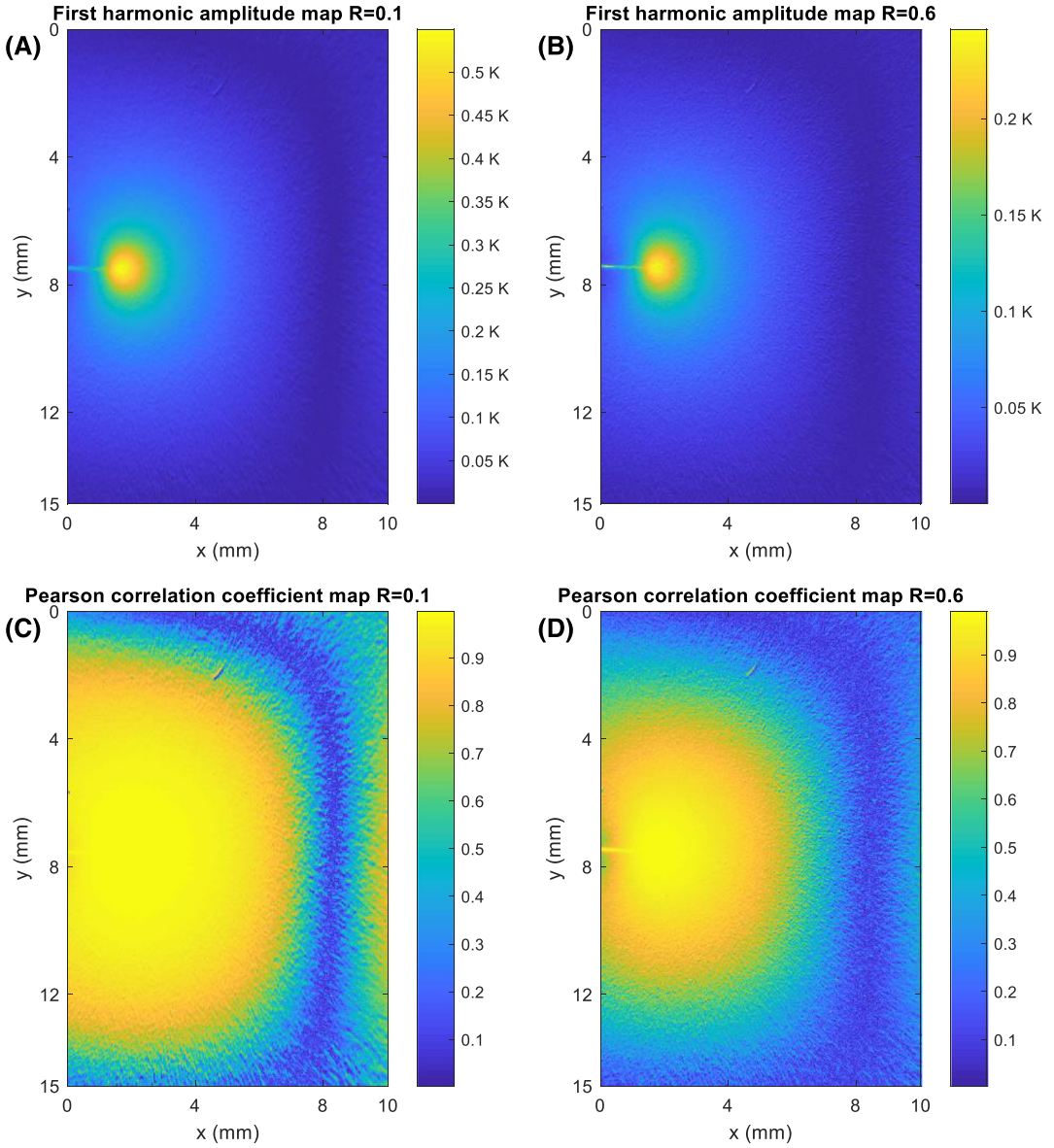

FIGURE 6 (A) First harmonic temperature amplitude map for a stress ratio of 0.1; (B) first harmonic temperature amplitude map for a stress ratio of 0.6; (C) Pearson's correlation coefficient map for a stress ratio of 0.1; and (D) Pearson's correlation coefficient map for a stress ratio of 0.6. All maps for a crack length of 8.5 mm [Colour figure can be viewed at wileyonlinelibrary.com]

of reference temperature on the temperature amplitude maps, they were normalized using the reference temperature, T_0. Data for stress intensity calculations were extracted from these maps at discrete points in an annular array that avoided inclusion of any nonlinear data and the high-strain gradient zones where adiabatic conditions may not be satisfied (see Figure 8). The techniques used in choosing these array points are explained below.

As these data must be referenced relative to the crack tip (the coordinate system origin) to calculate stress intensity values, the mesh center was taken as the maximum value point seen in Figure 7. An inaccurate location of this value might lead to an error in computed crack tip parameters. To bypass this problem, the crack tip location was included in the fitting algorithm. The inner radius of the annular array was calculated through the Dugdale approximation for plastic zone size[40] (Equation 22). Representative values of this variable of 2.20 mm and 5.63 mm were obtained for the minimum and maximum crack lengths used in the analysis. The Dugdale equation provides an overestimation of the plastic zone and hence removes the risk of partial inclusion of plastic data in the data fitting collection region. The outer radius was determined as the point where the temperature amplitude profile drops to zero before increasing again, as shown in Figure 7. A linear distribution of

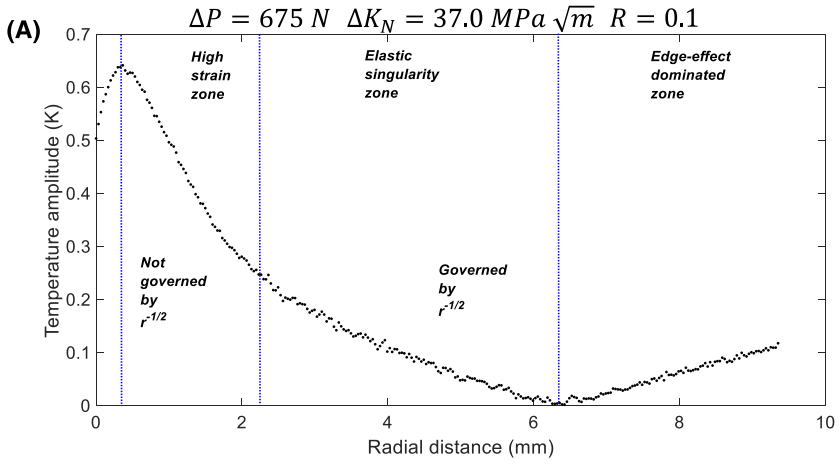

FIGURE 7 Temperature amplitude (signal peak-mean value M_1) profile along the crack growth direction for a stress ratio of (A) 0.1 and (B) 0.6. Displayed SIFs ranges correspond to nominal values. [Colour figure can be viewed at wileyonlinelibrary.com]

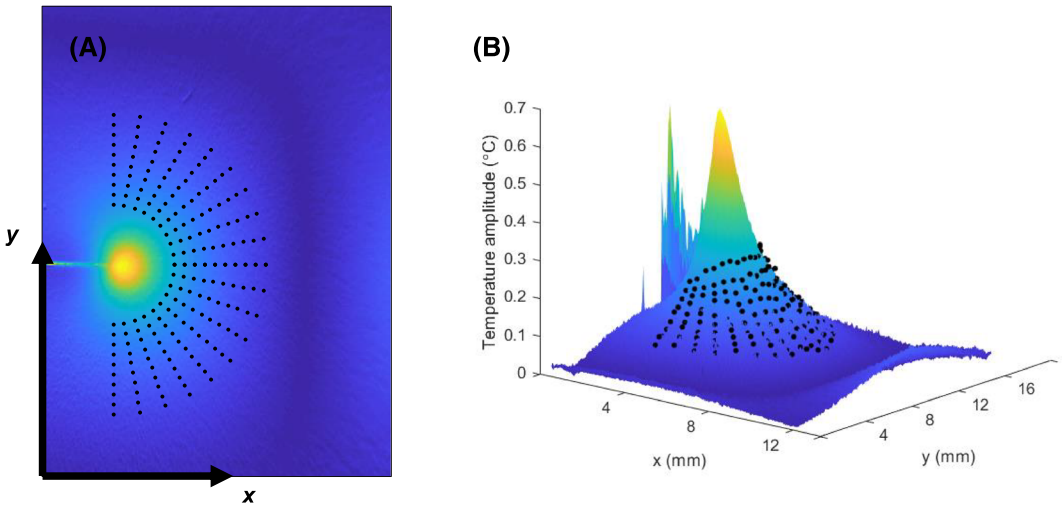

FIGURE 8 Annular array of data used in the fitting process. (A) 2D map view and (B) 3D surface view [Colour figure can be viewed at wileyonlinelibrary.com]

measurement points was selected with 10 points per line and 20 lines equally distributed over the 180° mesh. The fitting process therefore used an array of 200 points.

$$r_p = \frac{\pi}{8}\left(\frac{K_I}{S_y}\right)^2. \tag{22}$$

To fit the temperature data with the analytical equation used to evaluate the crack tip parameters, the nonlinear nature of Equation (15) required the adoption of a nonlinear optimization approach. As the temperature amplitude data were to be fitted to two different crack tip field models (Irwin–Westergaard and CJP), two different objective functions were defined. Error functions for the CJP model and for the Irwin–Westergaard model are shown in Equations (23) and (24), respectively.

$$\text{CJP}: \min_{\Delta A,\Delta B,\Delta C,\Delta E,\Delta F,\ \delta_x,\delta_y} \left\| \left(\frac{\Delta T}{T_0}\right)^{CJP} - \left(\frac{\Delta T}{T_0}\right)^{exp} \right\|_2, \quad (23)$$

$$\text{Irwin} - \text{Westergaard}: \min_{\Delta K_I,\Delta K_{II},\Delta T_x,\delta_x,\delta_y} \left\| \left(\frac{\Delta T}{T_0}\right)^{West} - \left(\frac{\Delta T}{T_0}\right)^{exp} \right\|_2. \quad (24)$$

In these equations, $\left(\frac{\Delta T}{T_0}\right)^{CJP}$ and $\left(\frac{\Delta T}{T_0}\right)^{West}$ are the analytical expressions of the normalized temperature range for the CJP model (Equations 5–7 into Equation 15) and the Westergaard model (Equations 2–4 into Equation 15), while $\left(\frac{\Delta T}{T_0}\right)^{exp}$ is the experimentally measured data, δ_x and δ_y are the crack tip location, and double vertical bars denote the operator norm. It is important to note that to obtain the range or peak-to-peak values of the crack tip parameters, twice the normalized amplitude must be used ($\Delta T = 2M_1$).

To reduce computational time, the crack tip position was searched within a predefined region. This region was calculated relative to the origin of the annular mesh by considering a square window of size 15 pixel (0.5 mm). This necessitates adding two constraints to both optimization problems. The Interior Point Algorithm was selected to solve these optimization problems.[41] This deterministic gradient-based method was then implemented via a quasi-Newton approach. Thus, the objective function gradient was computed using second-order finite differences (central derivative) and the Hessian matrix, employing the Broyden–Fletcher–Goldfarb–Shanno (BFGS) algorithm which is an iterative method for solving unconstrained nonlinear optimization problems.[42–44] Each optimization subproblem was solved by via a trust region method using a conjugate gradient approach. The trust-region method is one of the most important numerical optimization methods in solving nonlinear programming problems. It works by first defining a region around the current initial solution, in which the applied model can, to a first approximation, represent the original objective function. Initial solutions were generated from empirical and numerical correlations[45] for the stress intensity factor and the nonsingular stress along the crack growth direction in a CT specimen as shown in Equations (25) and (26).

$$K_N = \frac{P}{q\sqrt{W}} \frac{2+\alpha}{(1-a)^{\frac{3}{2}}} \left[0.886 + 4.64\alpha - 13.32\alpha^2 + 14.72\alpha^3 - 5.6\alpha^4\right], \quad (25)$$

$$T_N = \frac{K_{I,N}}{\sqrt{\pi q}} \left[0.1477 + 0.93746\beta - 0.87183\beta^2 + 0.35186\beta^3\right]. \quad (26)$$

In these equations, P is the applied load, q is the specimen thickness, W is the specimen width, α is the crack length normalized by the specimen width, β is the specimen thickness normalized by the width, K_N is the nominal stress intensity factor, and T_N is the nominal nonsingular stress along the crack growth direction. The crack length, which is necessary to define these values, was obtained employing a method based on the analysis of the vertical displacements measured with DIC. This method allows the crack tip to be obtained in the displacement maps and to calculate the corresponding crack length using the pixel–mm relationship. This method is fully explained in the work of Vasco-Olmo.[46] When using the Irwin–Westergaard approach, these values were directly included into the algorithm. For the CJP model, relationships between nominal values and the CJP coefficients were derived assuming that there is no shielding effect on the elastic field.[21] Thus, initial coefficients supplied to the solution algorithm are given by the following expressions:

$$\Delta A = -\Delta B = \frac{K_N(1-R)}{\sqrt{8\pi}}, \quad (27)$$

$$\Delta E = 0, \quad (28)$$

$$\Delta C = -\Delta F = T_N(1-R). \quad (29)$$

For the crack tip position, the initial supplied value was the annular mesh center employed during the data collection process.

4.2 | Calculation of thermal constants

As mentioned in Section 3, a 25 × 100 × 1 mm flat plate of commercially pure titanium was used to calculate the

TABLE 4 Loading cases used for thermal calibration and statistical values of the temperature in the ROI used for calibration

Loading case	Amplitude load (N)	Mean load (N)	$\mu(\Delta T/T_0)$	$s(\Delta T/T_0)$	$\frac{s}{\mu}(\Delta T/T_0)$
1	700	1400	5.5213E−04	5.9095E−06	0.01070310
2	700	1600	5.5715E−04	4.0155E−06	0.00720722
3	700	1800	5.5715E−04	4.0155E−06	0.00720722
4	1000	1400	7.6609E−04	3.8791E−06	0.00506350
5	1000	1600	7.6358E−04	4.1196E−06	0.00539511
6	1000	1800	7.6840E−04	5.0197E−06	0.00653267
7	1200	1400	9.1200E−04	4.5539E−06	0.00499331
8	1200	1600	9.1857E−04	4.6660E−06	0.00507963
9	1200	1800	9.2572E−04	4.0124E−06	0.00433436

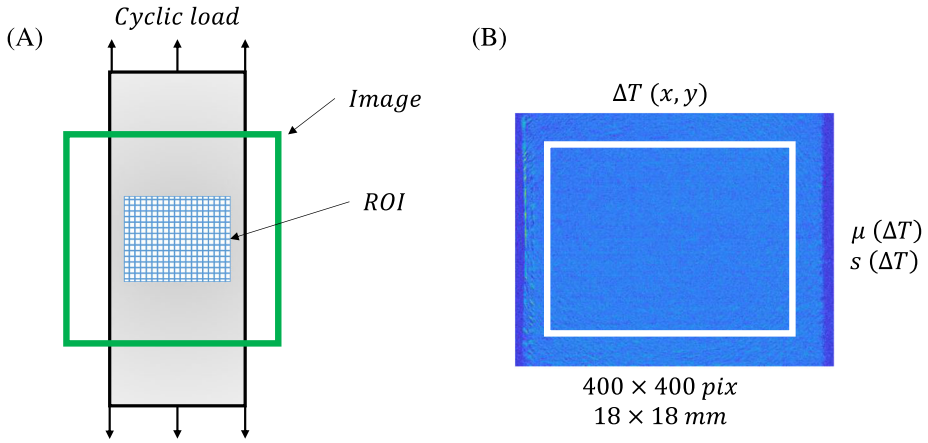

FIGURE 9 (A) Illustration of the region of interest (ROI) in the calibration specimen and (B) dimensions of the ROI demarcated with white lines, superimposed on an amplitude map [Colour figure can be viewed at wileyonlinelibrary.com]

thermoelastic constants. The plate specimen provides a uniaxial stress state to relate the applied stress range with the temperature variation.[33,35,36] Nine stress levels were used in the calibration, with different amplitudes and mean stresses (Table 4). Temperature amplitudes were calculated from the temperature maps, and a suitable region of interest (Figure 9) was defined to calculate the value of the thermoelastic constants. This region was defined centered at the plate, far from the loading points and avoiding corners where lens distortion might occur, as well as far from the plate edges where the temperature field may experience edge effects.

In Table 4, μ and s denote the mean and the standard deviation of the normalized temperature amplitude. The last column in Table 3 shows the Pearson variation coefficient for the temperature data, with values <1%. This means that the measurement dispersion is very low, and hence, the temperature distribution is uniform and constant in the region of interest.

To fit the calibration constants, Equation (16) must be simplified to fit the test case of uniaxial loading. In addition, this equation is reorganized through division by the alternating stress to obtain the equation of a straight line. The normalized temperature amplitude for the uniaxial loading case is then given by Equation (30).

TABLE 5 Experimentally determined thermoelastic constants

γ (1/MPa)	b (1/MPa^2)
3.1765×10^{-6}	4.3715×10^{-9}

$$\frac{\Delta T}{2T_0\sigma_a} = \gamma + b \cdot \sigma_m, \tag{30}$$

where σ_a is the stress amplitude and σ_m is the mean stress component. Calibration parameters were then obtained through a linear least squares fit to the line. The constants γ and b obtained by this process are shown in Table 5.

4.3 | Determination of crack tip parameters from DIC data

The procedure for determining crack tip parameters from DIC data is similar to the method that has been explained

for the TSA data. Displacement maps were obtained using commercial DIC software (VIC2D provided by Correlated Solutions Inc). The data points used in the fitting process were extracted from both horizontal and vertical displacement maps as shown in Figure 10. The inner mesh radius was calculated employing the Dugdale plastic radius approximation.[40] The outer radius was defined by analyzing vertical displacement contours as reported by Vasco-Olmo et al.[47] When displacement data are used for crack tip parameter determination, three additional parameters that take into account any rigid body motion displacement experienced by the specimen should be included into the fitting problem. Hence, employing a small-displacement correction, these three parameters are a horizontal displacement u_0, a vertical displacement v_0, and an in-plane rotation R_{xy}.

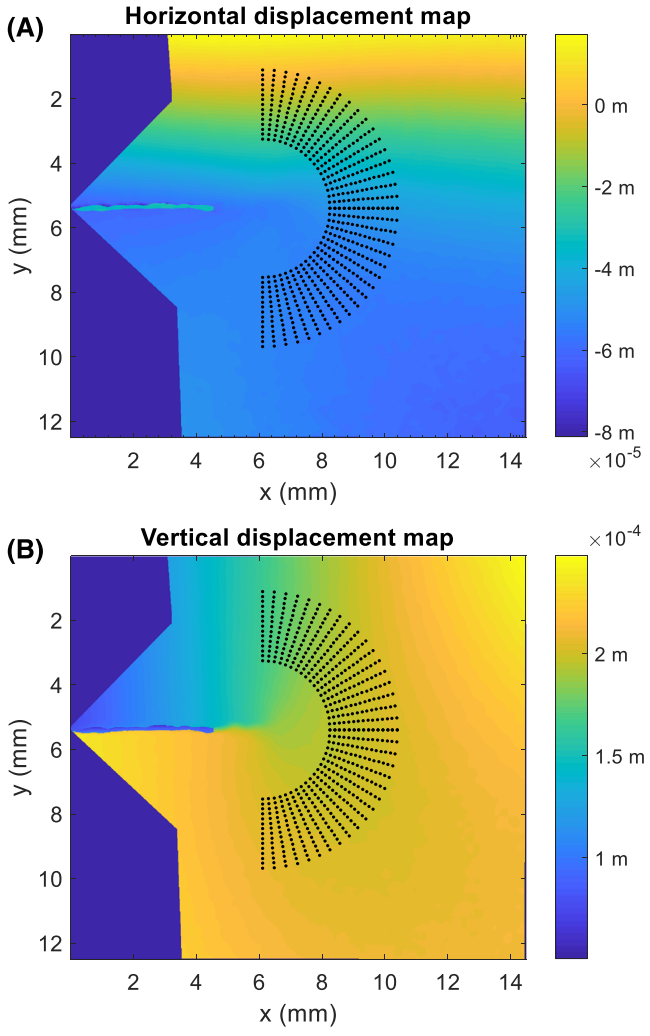

FIGURE 10 Annular set of measurement data points shown superimposed on (A) the horizontal displacement map and (B) the vertical displacement map. Maps for a crack length of 8.5 mm [Colour figure can be viewed at wileyonlinelibrary.com]

$$\min_{A,B,C,E,F,\ \delta_x,\delta_y,u_0,v_0,R_{xy}} \left\| (u+jv)^{CJP} - (u+jv)^{exp} \right\|_2. \quad (31)$$

For DIC data, both maximum and minimum load maps were processed and crack tip parameters were calculated as the difference between the maximum and the minimum loads. Initial solution values were determined in a similar fashion to TSA data processing (Equations 25–29), and the initial rigid body motion coefficients were set as zero.

5 | RESULTS AND DISCUSSION

Figure 11 shows the experimentally measured values of ΔK_F for the CJP model and ΔK_I for the Irwin–Westergaard model. These have been calculated from TSA and DIC data for each of the two stress ratios of 0.1 and 0.6 and are shown together with a line that plots the standard stress intensity solution for a CT specimen, given in ASTM E647.

For the higher stress ratio $R = 0.6$, the absolute values of SIF range obtained using TSA are very similar for both the Irwin–Westergaard (ΔK_I) and CJP (ΔK_F) models and are also close to the ASTM standard CT stress intensity solution line. This is perhaps not surprising, as there would be expected to be only a minor influence on crack growth from plasticity-induced shielding. Table 6 shows that the relative difference between the average values of the TSA and DIC solutions and the standard value is all relatively small, TSA value differences of 2.99% (CJP) and 2.45% (Westergaard) and a CJP DIC difference of 3.67%.

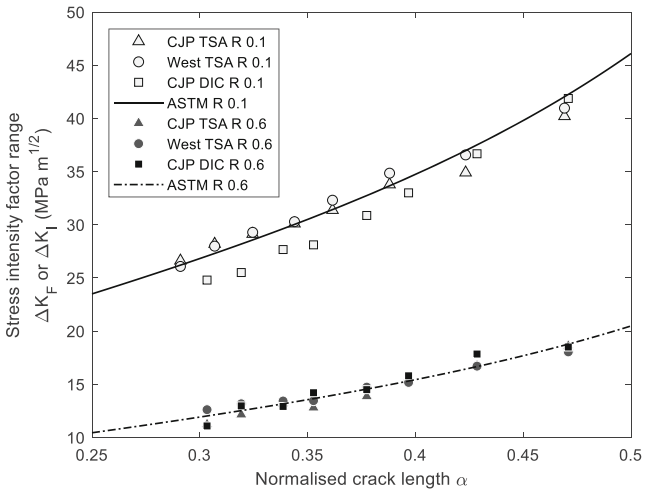

FIGURE 11 Stress intensity factor ranges ΔK_I or ΔK_F obtained by TSA and DIC data plotted versus the normalized crack length for the two different stress ratios of 0.1 and 0.6

TABLE 6 SIF value ΔK error (%) relative to the standard definition

			TSA				DIC	
Crack length (mm)	**ASTM $R = 0.1$**	**ASTM $R = 0.6$**	**CJP $R = 0.1$**	**CJP $R = 0.6$**	**West $R = 0.1$**	**West $R = 0.6$**	**CJP $R = 0.1$**	**CJP $R = 0.6$**
5.82	26.21	12.02	+1.58	−6.59	−0.47	+4.91	−8.34	−7.80
6.13	27.31	12.53	+3.25	−3.01	+2.50	+5.13	−9.51	+3.55
6.49	28.60	13.17	+1.94	+0.14	+2.51	+2.01	−6.61	−1.87
6.87	30.03	13.65	−0.25	−6.20	+0.86	−1.40	−8.49	+4.08
7.23	31.43	14.55	+0.14	−4.70	+2.81	+1.27	−5.70	−0.35
7.76	33.70	15.31	+0.37	+1.90	+3.55	−0.85	−4.20	+3.21
8.46	37.00	16.67	−5.60	+0.51	−1.09	−0.24	−2.21	+7.07
9.38	42.04	18.78	−4.37	−0.89	−2.55	−3.88	−0.89	−1.44
Mean abs value	—	—	2.18	2.99	2.04	2.45	5.74	3.67

Note: Crack length is defined from specimen holes.

Inspection of the values in Table 6 as a function of crack length indicates a more significant variation as the shielding contribution changes during crack growth.

At the lower stress ratio value of $R = 0.1$, a greater relative percentage difference is observed in the CJP DIC data compared with the standard solution, and as the ΔK values are higher than at $R = 0.6$, the difference can be easily observed in Figure 11. This would be expected, as the CJP model incorporates plasticity-induced shielding influences in the calculated values of both K_F and K_R. In the case of the driving force K_F, this is primarily plastic blunting that reduces it, while for K_R, crack wake contact and compatibility-induced strains are more important and their interaction can provide a stress intensity that either retards or accelerates crack growth. Average percentage differences from the standard solution at $R = 0.1$ are given in Table 6 as 2.18% for the case of the CJP model using TSA, 2.04% for the TSA solution using the Irwin–Westergaard model, and 5.74% for the CJP model using DIC. As expected, the results obtained using the Irwin–Westergaard approach and TSA data agree closely with the standard value at both values of R due to the linear elastic nature of the model. The CJP model, based on a more inclusive capture of the influences of the plastic zone surrounding the crack, which are relatively small for this titanium alloy, gives a more informative picture as discussed above and the relative differences between its predictions of ΔK_F obtained with either TSA or DIC agree very well at $R = 0.6$ and slightly less well at $R = 0.1$. This may reflect at the necessity for a slight tweaking of the higher order terms used in TSA model to identify the effects of plasticity on crack growth. Nonetheless, the approach outlined in this paper offers a very significant step forward in applying TSA to crack growth in the presence of plasticity. However, it has been

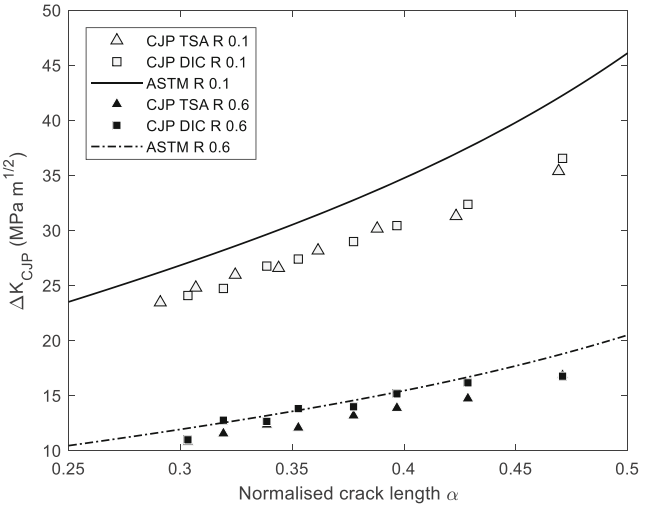

FIGURE 12 Plot of the CJP model effective range of stress intensity factor, calculated using Equation (31) for both DIC and TSA data, versus the normalized crack length for the cases of $R = 0.1$ and 0.6

previously shown[24] that the range of K_F is insufficient to quantify the fatigue crack driving force since the CJP model provides a more comprehensive crack tip shielding influence through the ΔK_{CJP} by combining ΔK_F and ΔK_R as shown in Equation (1) which is repeated here for convenience. In this equation, the sign of K_R matters in terms of either assisting or retarding crack growth, and this is based on the direction assigned to it as a retarding force on the elastic field in the original mathematical derivation.[23] Thus, as reported by Vasco-Olmo et al.,[24] negative values retard the crack growth ($K_F - |K_R|$) and positives values enhance the crack growth ($K_F + |K_R|$). The correct direction is pointing back to the crack origin, and a positive value then makes it a retarding force on

the elastic field. In the discussion in this paper, however, as TSA data are stored as an absolute value, that is, sign-free, the absolute values of ΔK_R will be used in Equation (1), changing it to

$$\Delta K_{CJP} = \Delta K_F - |\Delta K_R|. \tag{32}$$

Figure 12 shows a plot of ΔK_{CJP} versus the normalized crack length for both the DIC and TSA data and at both stress ratios.

Figure 12 demonstrates that the differences observed in Figure 11 at $R = 0.1$ in the stress intensity factor range measured with the TSA and DIC techniques have now been eliminated when data are plotted using the ΔK_{CJP} instead of the ΔK_F parameter. It should be noted that this graph is not plotted against crack growth rate, da/dN, and therefore, the growth rate curves do not coincide at the two stress ratio values. The close correspondence of the ΔK_{CJP} values for TSA and DIC with ΔK_F, while the ΔK_R values are different (see Figure 13), can be mathematically explained by considering the coefficient E that models part of the shielding effect. E is included in the formulation of both K_F and K_R, and a comprehensive crack shielding influence should be quantified through the inclusion of both parameters that then gives its complete influence. The ΔK_{CJP} values have a fairly uniform difference of approximately 13% compared with the standard solution at $R = 0.1$. At $R = 0.6$, a more variable but smaller difference of ≈5% (lower than the standard solution) was observed.

Figure 13 shows the absolute values of the retardation stress intensity factor range (ΔK_R) plotted as a function of the normalized crack length. At the higher R value, similar values are observed for ΔK_R using either TSA or DIC techniques, as the shielding will be limited. Larger differences were observed at the lower stress ratio $R = 0.1$, particularly of normalized crack length <0.42. Those differences might be attributed to the influence of coefficient E in both K_F and K_R and hence on their corresponding stress terms ($z^{-1/2}$ and $z^{-1/2}\ln z$). However, as shown in Figure 12, when a comprehensive parameter as ΔK_{CJP} is used (gives the full influence of both stress terms), differences are removed. Figure 13 also shows that ΔK_R values increase as the crack grows demonstrating how the plasticity-induced crack shielding effect increases as the crack length increases. Figure 14 compares ΔK_{CJP} values obtained with the two techniques (TSA and DIC) and a perfect agreement would follow the straight line at 45°. The plot also shows 5% deviation lines, and it is clear that the data fall inside this band (mean difference of 2.3% for $R = 0.1$ and 4.1% for $R = 0.6$).

Finally, the fit quality for TSA data represented with the Pearson correlation coefficient is shown in Figure 15 for both the Irwin–Westergaard approach and the CJP model. It shows the Pearson correlation coefficient between experimental TSA data (peak-to-peak temperature) and the theoretically fitted data obtained by reconstructing the peak-to-peak temperature map through the analytical equations for the two models.

Figure 15 illustrates three significant points. First, the correlation coefficients are higher than 98.5% with either model, any crack length, and both stress ratio values, demonstrating that the experimental and theoretical data agree very well. Second, correlation coefficients for the low-stress ratio (higher temperature amplitude) are higher than for the lower amplitude data. This fact could be due

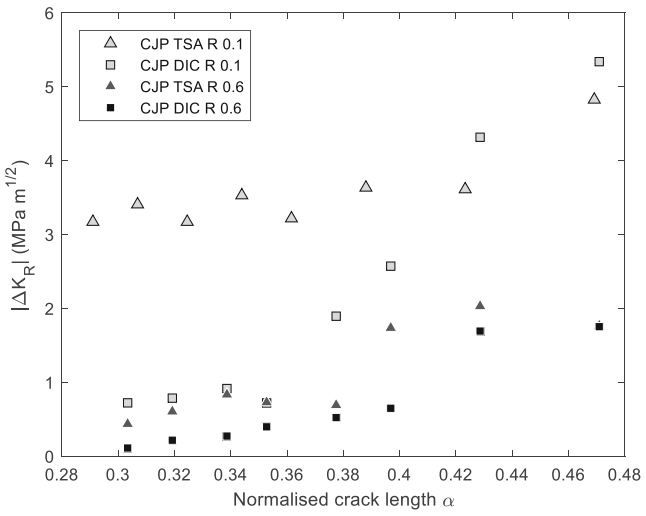

FIGURE 13 Values of the retardation stress intensity factor range ΔK_R plotted as a function of the normalized crack length for both TSA and DIC data and at both stress ratio values

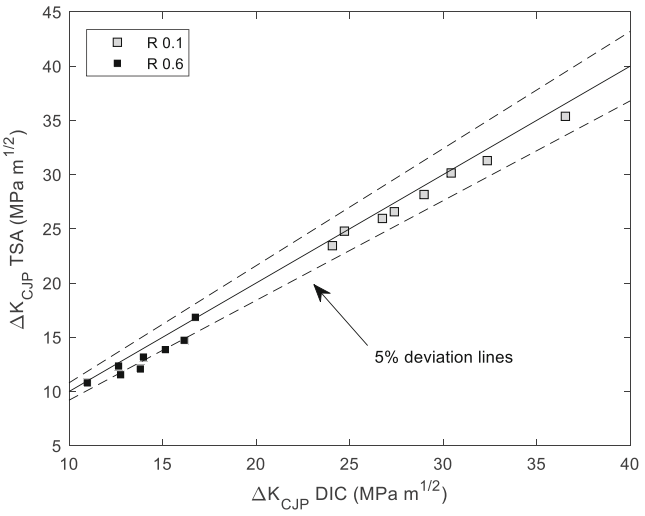

FIGURE 14 Comparison between the stress intensity factors ranges obtained using the CJP model and the TSA and DIC techniques

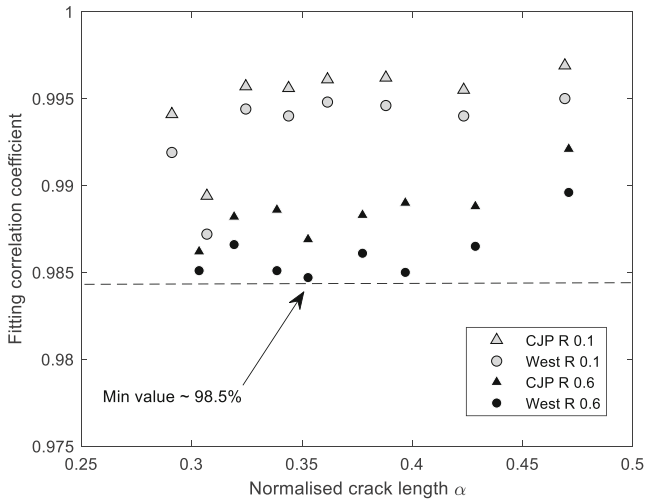

FIGURE 15 Fitting quality correlation coefficient for the TSA data from both models (CJP and Irwin–Westergaard) and both stress ratios, compared with the experimental peak-to-peak temperature map

to a higher noise in the lower temperature amplitude data since smaller temperature measurements commonly implies a noisier signal. This can be also observed in Figure 6 where temperature amplitude maps are better shaped for higher amplitudes. The third and the most important point is that the correlation coefficient using the CJP model always provides a better fit to the experimental data than the Irwin–Westergaard approach. This is interpreted as highlighting the improved ability of the CJP model to capture the influence of plasticity on the global stress field surrounding a fatigue crack in contrast to purely elastic-based models such as Irwin–Westergaard.

6 | CONCLUSIONS

This work proposes a method for calculating crack tip stress parameters using a high-order thermoelastic formulation that allows at least partial capture of the influence of plasticity. The proposed technique was validated against digital image correlation data and compared with the purely elastic Irwin–Westergaard model and with the CJP model of crack tip fields that includes the plasticity-induced shielding effects. The results in terms of the range of stress intensity factor and fitting quality parameters demonstrate the improved capability of the CJP model in characterizing the crack tip stress field when the plastic enclave surrounding the crack affects the global stress field and induces a retardation/acceleration effect on the fatigue crack growth rate. The work has demonstrated that the TSA approach can identify a plasticity influence in the crack tip field, provided that higher order terms are used, and that the technique can then be fitted to the CJP model to yield K_F and K_R terms. In this initial work, only two stress terms are used in the TSA equation, following the approach of Di Carolo et al.[33] It is possible that further work would identify additional higher order terms that would increase the accuracy of the TSA approach, albeit with an increased complexity in the analysis. Hence, potential future work could include the analysis of variable amplitude loading during fatigue crack growth by analyzing not only the CJP model parameters but also going deeper into high-order harmonics that appear as the consequence of high-magnitude nonlinear effects.

ACKNOWLEDGMENT

The authors want to acknowledge the financial support from Junta de Andalucía through the research project "1380786" funded by the program "Proyectos de I + D + i en el Marco del Programa Operativo FEDER Andalucía 2014-2020.

DATA AVAILABILITY STATEMENT

The data that support the findings of this study are available from the corresponding author upon reasonable request.

NOMENCLATURE

$\sigma_x, \sigma_y, \tau_{xy}$	Plane stress tensor (MPa)
r, θ	Polar coordinates (mm, rad)
K_I	Opening mode stress intensity factor (MPa $\sqrt{m}$)
K_{II}	In-plane shear mode stress intensity factor (MPa $\sqrt{m}$)
T_x	Nonsingular stress along the crack growth direction (MPa)
A, B, C, E, F	CJP model coefficients (MPa $\sqrt{m}$, MPa)
K_F	CJP model opening mode stress intensity factor that drives growth forwards (MPa $\sqrt{m}$)
$K_{F,max}$	CJP opening mode stress intensity factor that drives growth forward at maximum load (MPa $\sqrt{m}$)
$K_{F,min}$	CJP opening mode stress intensity factor that drives growth forward at minimum load (MPa $\sqrt{m}$)
K_R	CJP model stress intensity factor that acts to retard crack growth (MPa $\sqrt{m}$)
$K_{R,max}$	CJP model stress intensity factor that acts to retard crack growth at maximum load (MPa $\sqrt{m}$)

$K_{R,min}$	CJP model stress intensity factor that acts to retard crack growth at minimum load (MPa $\sqrt{\text{m}}$)
K_S	CJP model shear stress intensity factor (MPa $\sqrt{\text{m}}$)
ΔK	Irwin stress intensity factor range (MPa $\sqrt{\text{m}}$)
ΔK_{CJP}	CJP model effective SIF range (MPa $\sqrt{\text{m}}$)
T_y	Nonsingular stress along the crack opening direction (MPa)
u, v	Plane displacement field (mm)
z	Complex variable (mm)
j	Imaginary unit ($\sqrt{-1}$)
G	Shear modulus (GPa)
ν	Poisson's coefficient
κ	Variable dependent on either plane stress or plane strain conditions
ΔT	Temperature range (°C)
T_0	Reference temperature (°C)
γ, b	Thermoelastic constants ($1/\text{MPa}, 1/\text{MPa}^2$)
$\Delta\sigma_I, \Delta\sigma_{II}$	Principal stresses ranges (MPa)
R	Stress ratio
R_f	Stress ratio function
$\Delta\sigma_x, \Delta\sigma_y, \Delta\tau_{xy}$	Plane stress tensor components ranges (MPa)
$T(t)$	Temperature signal (°C)
M_r	Temperature rate (°C/s)
M_i	i^{th} harmonic amplitude (°C)
ω	Angular frequency (rad/s)
ϕ_i	i^{th} harmonic phase (rad)
t	Time (s)
i	Sum index
m_i, n_i	Amplitude components (°C)
δ_x, δ_y	Crack tip coordinates (mm)
r_p	Dugdale plastic radius (mm)
S_y	0.2% Yield Stress (MPa)
K_N	Irwin stress intensity factor (MPa $\sqrt{\text{m}}$)
T_N	Nonsingular T-stress (MPa)
α	Normalized crack length
β	Normalized thickness
P	Applied load (N)
W	Specimen width (mm)
q	Specimen thickness (mm)
$\Delta A, \Delta B, \Delta C, \Delta E, \Delta F$	CJP model coefficients ranges (MPa $\sqrt{\text{m}}$, MPa)
μ, s	Mean and standard deviation
σ_a, σ_m	Alternating and mean stress components (MPa)
u_0, v_0, R_{xy}	Rigid body motion coefficients (mm, rad)
ΔK_I	Mode I Irwin–Westergaard stress intensity range (MPa $\sqrt{\text{m}}$)
ΔK_F	CJP mode opening mode SIF range (MPa $\sqrt{\text{m}}$)
ΔK_R	CJP model retardation SIF range (MPa $\sqrt{\text{m}}$)

ORCID

Alonso Camacho-Reyes https://orcid.org/0000-0002-7524-0039

Jose M. Vasco-Olmo https://orcid.org/0000-0002-2250-2306

Francisco A. Diaz https://orcid.org/0000-0003-0467-542X

REFERENCES

1. Paris PC, Gomez MP, Anderson WP. A rational analytic theory of fatigue. *Trend Eng*. 1961;13:9-14.
2. Elber W. Fatigue crack closure under cyclic tension. *Eng Fract Mech*. 1970;2(1):37-44.
3. Elber W. *The Significance of Fatigue Crack Closure*. ASTM Spec Tech Publ; 1971:230-242.
4. Ritchie RO. Mechanisms of fatigue crack propagation in metals, ceramics and composites: role of crack tip shielding. *Mater Sci Eng A*. 1988;103(1):15-28.
5. Pippan R, Hohenwarter A. Fatigue crack closure: a review of the physical phenomena. *Fatigue Fract Eng Mater Struct*. 2017;40(4):471-495.
6. Fleck NA, Smith RA. Crack closure—is it just a surface phenomenon? *Int J Fatigue*. 1982;4(3):157-160.
7. James MN, Knott JF. Critical aspects of the characterization of crack tip closure by compliance techniques. *Mater Sci Eng A*. 1985;72(1):L1-L4.
8. James MN. Some unresolved issues with fatigue crack closure. In: *Proceedings of the 9th International Conference on Fracture*. Sydney, Australia: Advances in Fracture Mechanics; 1997:2403-2414.
9. Allison J, Ku R, Pompetzki M. A comparison of measurement methods and numerical procedures for the experimental characterization of fatigue crack closure. In: *Mechanics of Fatigue Crack Closure*. Baltimore: ASTM International; 2009:171-171–15.
10. Jones JW, Macha DE, Corbly DM. Observations on fatigue crack opening load determinations. *Int J Fract*. 1978;141:R25-R30.
11. Nurse AD, Patterson EA. Photoelastic determination of fatigue-crack stress intensity factors. In: Valley, MT and DelGrande, NK and Kobayashi A, ed. Nondestructive Inspection of Aging Aircraft. Vol 2001. Proceedings of the Society of Photo-Optical Instrumentation Engineers (SPIE). PO Box 10, Bellingham, WA 98227–0010: SPIE - INT SOC OPTICAL ENGINEERING; 1993:155–162.
12. Pacey MN, James MN, Patterson EA. A new photoelastic model for studying fatigue crack closure. *Exp Mech*. 2005;451:42-52.
13. Sutton MA, Orteu JJ, Schreier HW. *Image Correlation for Shape, Motion and Deformation Measurements*. New York: Springer US; 2009.

14. Rabbolini S, Beretta S, Foletti S, Cristea ME. Crack closure effects during low cycle fatigue propagation in line pipe steel: an analysis with digital image correlation. *Eng Fract Mech*. 2015;148:441-456.
15. Lopez-Crespo P, Shterenlikht A, Yates JR, Patterson EA, Withers PJ. Some experimental observations on crack closure and crack-tip plasticity. *Fatigue Fract Eng Mater Struct*. 2009; 32(5):418-429.
16. Nowell D, Paynter RJH, De Matos PFP. Optical methods for measurement of fatigue crack closure: Moiré interferometry and digital image correlation. *Fatigue Fract Eng Mater Struct*. 2010;33(12):778-790.
17. Thomson W, Lord K. On the thermoelastic, thermomagnetic and pyro-electric properties of matters. *Philos Mag*. 1878;5(28): 4-27.
18. Diaz FA, Patterson EA, Tomlinson RA, Yates JR. Measuring stress intensity factors during fatigue crack growth using thermoelasticity. *Fatigue Fract Eng Mater Struct*. 2004;27(7): 571-583.
19. De Matos PFP, Nowell D. Analytical and numerical modelling of plasticity-induced crack closure in cold-expanded holes. *Fatigue Fract Eng Mater Struct*. 2008;31(6):488-503.
20. Diaz FA, Vasco-Olmo JM, Lopez-Alba E, Felipe-Sese L, Molina-Viedma AJ, Nowell D. Experimental evaluation of effective stress intensity factor using thermoelastic stress analysis and digital image correlation. *Int J Fatigue*. 2020;135: 105567.
21. Christopher CJ, James MN, Patterson EA, Tee KF. Towards a new model of crack tip stress fields. *Int J Fract*. 2007;148(4): 361-371.
22. Christopher CJ, James MN, Patterson EA, Tee KF. A quantitative evaluation of fatigue crack shielding forces using photoelasticity. *Eng Fract Mech*. 2008;75(14):4190-4199.
23. James MN, Christopher CJ, Lu YW, Patterson EA. Local crack plasticity and its influences on the global elastic stress field. *Int J Fatigue*. 2013;46:4-15.
24. Vasco-Olmo JM, Yang B, James MN, Diaz FA. Investigation of effective stress intensity factors during overload fatigue cycles using photoelastic and DIC techniques. *Theor Appl Fract Mech*. 2018;97:73-86.
25. Yang B, Vasco-Olmo JM, Díaz FA, James MN. A more effective rationalisation of fatigue crack growth rate data for various specimen geometries and stress ratios using the CJP model. *Int J Fatigue*. 2018;114:189-197.
26. Pippan R, Riemelmoser FO. Visualization of the plasticity-induced crack closure under plane strain conditions. *Eng Fract Mech*. 1998;60(3):315-322.
27. Vasco-Olmo JM, James MN, Christopher CJ, Patterson EA, Diaz FA. Assessment of crack tip plastic zone size and shape and its influence on crack tip shielding. *Fatigue Fract Eng Mater Struct*. 2016;39(8):969-981.
28. Nowell D, Nowell SC. A comparison of recent models for fatigue crack tip deformation. *Theor Appl Fract Mech*. 2019; 103:102299.
29. Pommier S, Hamam R. Incremental model for fatigue crack growth based on a displacement partitioning hypothesis of mode I elastic-plastic displacement fields. *Fatigue Fract Eng Mater Struct*. 2007;30(7):582-598.
30. Westergaard HM. Bearing pressures and cracks. *J Appl Mech*. 1939;61(2):49-53.
31. Irwin GR. Analysis of stresses and strains near the end of a crack traversing plate. *J Appl Mech*. 1957;24(3):361-370.
32. Muskhelishvili NI. *Some Basic Problems of the Mathematical Theory of Elasticity*. Netherlands: Springer; 1977.
33. Di CF, De FR, Palumbo D, Galietti U. A thermoelastic stress analysis general model: study of the influence of biaxial residual stress on aluminium and titanium. *Met*. 2019;9:671.
34. Robinson AF, Dulieu-Barton JM, Quinn S, Burguete RL. The potential for assessing residual stress using thermoelastic stress analysis: a study of cold expanded holes. *Exp Mech*. 2012;53: 299-317.
35. Palumbo D, Galietti U. Data correction for thermoelastic stress analysis on titanium components. *Exp Mech*. 2016;56(3): 451-462.
36. Palumbo D, De Finis R, Di Carolo F, Vasco-Olmo J, Diaz FA, Galietti U. Influence of second-order effects on thermoelastic behaviour in the proximity of crack tips on titanium. *Exp Mech*. 2021;62(3):1-15.
37. Boyer R, Collings EW, Welsch G. *Material Properties Handbook: Titanium Alloys*. ASM International; 1994.
38. Pitarresi G, Cappello R. Evaluation of crack-closure by second harmonic thermoelastic stress analysis. *Int J Fatigue*. 2022;164: 107116.
39. Sanford RJ, Dally JW. A general method for determining mixed-mode stress intensity factors from isochromatic fringe patterns. *Eng Fract Mech*. 1979;621:621-633.
40. Dugdale DS. Yielding of steel sheets containing slits. *J Mech Phys Solids*. 1960;8(2):100-104.
41. Waltz RA, Morales JL, Nocedal J, Orban D. An interior algorithm for nonlinear optimization that combines line search and trust region steps. *Math Program*. 2006;107(3):391-408.
42. Goldfarb D. A family of variable-metric methods derived by variational means. *Math Comput*. 1970;24(109):23-26.
43. Fletcher R, Powell MJD. A rapidly convergent descent method for minimization. *Comput J*. 1963;6(2):163-168.
44. Broyden CG. Quasi-Newton methods and their application to function minimisation. *Math Comput*. 1967;21(99):368-381.
45. Kudari SK, Kodancha KG. 3D stress intensity factor and T-stresses (T11 and T33) formulations for a compact tension specimen. *Frat Ed Integrità Strutt*. 2017;11:216-225.
46. Vasco-Olmo JM, Díaz Garrido FA, Antunes FV, James MN. Plastic CTOD as fatigue crack growth characterising parameter in 2024-T3 and 7050-T6 aluminium alloys using DIC. *Fatigue Fract Eng Mater Struct*. 2020;43(8):1719-1730.
47. Vasco-Olmo JM, Diaz FA, Patterson EA. Experimental evaluation of shielding effect on growing fatigue cracks under overloads using ESPI. *Int J Fatigue*. 2016;83:117-126.

How to cite this article: Camacho-Reyes A, Vasco-Olmo JM, James MN, Diaz FA. A higher order thermoelastic analysis of fatigue crack growth can assess crack tip shielding. *Fatigue Fract Eng Mater Struct*. 2023;46(4):1596-1612. doi:10.1111/ffe.13949